Corrosion Science 165 (2020) 108407

Contents lists available at ScienceDirect

Corrosion Science

journal homepage: www.elsevier.com/locate/corsci

Effect of structural order on oxidation kinetics and oxide phase evolution of Al–Zr alloys

Yifei Xu[a], Lars P.H. Jeurgens[b], Yuan Huang[a], Chong Li[a], Yongchang Liu[a], Zumin Wang[a,*]

[a] School of Materials Science and Engineering, Tianjin University, Tianjin, 300350, China
[b] Swiss Federal Laboratories for Materials Science and Technology, Laboratory for Joining Technologies and Corrosion, Ueberlandstrasse 129, 8600, Duebendorf, Switzerland

ARTICLE INFO

Keywords:
Oxidation
Oxidation kinetics
Structural disordering
Amorphous alloy
Al–Zr alloy

ABSTRACT

To reveal the fundamental role of structural order of the parent alloy on the oxidation mechanism, thermal oxidation of amorphous and crystalline Al–Zr alloys with identical compositions were investigated in detail. An $(Al_{0.68}Zr_{0.32})O_{1.66}$ amorphous oxide emerged on crystalline Al_2Zr, whereas an $(Al_{0.33}Zr_{0.67})O_{1.83}$ amorphous oxide formed on amorphous $Al_{68at.\%}Zr_{32at.\%}$ under the same conditions. Oxidation kinetics was fast and linear for crystalline Al_2Zr but slow and parabolic for amorphous $Al_{68at.\%}Zr_{32at.\%}$. The underlying mechanisms of such striking differences were disclosed by molecular dynamics simulations. The findings thus offer new prospects in the field of surface engineering.

1. Introduction

The oxide layer developing on an alloy surface during thermal oxidation influences many important material properties, such as corrosion resistance, catalytic activity, adhesion, friction, wear and long-term reliability, biocompatibility, conductivity, and optical properties [1–8]. The oxide layer produced on the alloy can be amorphous or crystalline, depending on numerous factors, such as the difference between the bulk Gibbs energies of the amorphous and crystalline states of the competing oxide phases, the participating surface and interface energies, the initial lattice mismatch with the parent substrate, the oxide layer thickness, the alloy composition, and the oxidation temperature [9–16]. Because of the relatively large free volume and bond flexibility of amorphous oxides, growth stresses and thermally induced stresses may be partly accommodated by viscous flow, thereby promoting adhesion across the substrate–film interface [9,17–20]. Moreover, the absence of grain boundaries and other lattice defects in amorphous oxides decreased the number of fast short-circuit diffusion paths, thereby promoting the formation of chemically and structurally homogeneous oxide layers of highly uniform thicknesses. Consequently, amorphous oxide layers often exhibit favourable properties unlike their crystalline counterparts, such as improved corrosion resistance [21] and high optical transparency [22]. For instance, oxidation-resistant amorphous coatings have been used to protect the metallic alloys in various corrosive environments [4,21]; amorphous oxides such as SiO_2 and Al_2O_3 are widely used as tunnelling barriers in microelectronics [23] and amorphous oxide semiconductors (e.g. In–Ga–Zn–O) are used in modern thin-film transistors [5].

Admittedly, one important downside of functional amorphous oxide layers is their limited thermodynamic stability at elevated temperatures, which is typically governed by the kinetic barrier for heterogeneous nucleation of the competing crystalline oxide phase(s) at the substrate–oxide interface [24]. In this regard, it is necessary to clarify how the crystallinity of the parent alloy substrate actually influences the formation and thermal stability of amorphous oxide layers on the parent alloy substrate by thermal oxidation. In other words, the thermal oxidation of an amorphous alloy of a given homogenous composition likely differs from its crystalline counterpart due to the disordered atomic arrangement and the lack of grain boundaries (GBs) and other lattice defects in the former. The role of GBs in the parent alloy in determining oxygen diffusion has been reported previously [25,26]: GBs provide short-circuit paths for enhanced outward diffusion of alloy constituents as well as fast inward diffusion of oxygen. Previous studies on the thermal oxidation of (hydrogenated) amorphous and (poly-) crystalline silicon indicate a significant effect of the crystallinity of the parent substrate on the growth kinetics and stress state of the developing amorphous SiO_2 film [27,28]. A systematic, comparative study on the thermal oxidation of an alloy of identical composition in its amorphous and crystalline state is needed to illustrate the fundamental role of atomic structure of the parent alloy on its oxidation behaviour.

* Corresponding author.
E-mail address: z.wang@tju.edu.cn (Z. Wang).

https://doi.org/10.1016/j.corsci.2019.108407
Received 11 July 2019; Received in revised form 18 November 2019; Accepted 18 December 2019
Available online 19 December 2019
0010-938X/

For such a comparative oxidation study, the alloy constituents should ideally exhibit a similar affinity for oxygen as well as comparable Gibbs energies of formation, $\Delta_f G^0$ (in kJ per mole oxygen), for the competing amorphous and crystalline oxide phase formation. As such, selective oxidation issues can be largely neglected. In this respect, the Al–Zr binary system is a highly suitable candidate because the alloy constituents (i.e. Al and Zr) have similar affinities towards oxygen and the Gibbs energies of formation (per mole of oxygen) for all competing amorphous and crystalline ZrO_2 and Al_2O_3 single-oxide phases are also comparable [24].

Weller *et al.* [14,29] systematically investigated the thermal oxidation of amorphous Al–Zr alloys in the temperature range of 350–400 °C (under atmospheric pressure), revealing the thermodynamically preferred formation of a stoichiometric amorphous $(Al_{0.33}Zr_{0.67})O_{1.83}$ phase over a large compositional range of the parent alloy. In this work, thermal oxidation of the am- $Al_{68at.\%}Zr_{32at.\%}$ solid solution was compared to that of the c-Al_2Zr intermetallic alloy with an identical composition, and the role of lattice disorder in the parent alloy in determining the evolution of the oxide phase during thermal oxidation was revealed.

2. Experimental and computational methods

2.1. Materials

The c-Al_2Zr ingots were prepared in a magnetic levitation melting furnace by melting pure Al (purity 99.999 wt.%) and pure Zr (purity 99.99 wt.%) under the protection of pure Ar gas (purity 99.995 vol.%, 0.4 bar). The raw mixture of (well-weighted) Al and Zr was melted at 1750 °C and solidified in the furnace repeatedly for 4 cycles to improve the purity and homogeneity of the alloy, and finally cast to form the c-Al_2Zr ingots. The thus-prepared c-Al_2Zr ingots were cut into pieces with dimensions of 5 × 10 × 2 mm^3, followed by polishing using a series of SiC (#600-#7000) and diamond (0.5–0.1 μm) abrasive papers until a mirror-like surface was obtained. After polishing, the specimens were ultrasonically cleaned sequentially in acetone and ethanol and finally dried by blowing with compressed N_2 gas.

The am-$Al_{68at.\%}Zr_{32at.\%}$ alloys were deposited on 50-nm Si_3N_4/50-nm SiO_2/Si(100) wafers by co-sputtering pure Al (purity ≥ 99.9995 wt.%, target power = 101 W) and Zr (purity ≥ 98.5 wt.%, target power = 100 W) targets in a high-vacuum sputter system (base pressure < 5 × 10^{-6} Pa), with a deposition rate of ~11 nm/min [29].

2.2. Thermal oxidation

The c-Al_2Zr specimens were sealed in quartz tubes for thermal oxidation in a vacuum sealing system (MRVS-3002, Partulab Technology Co. Ltd). The tubes were first evacuated (base pressure ~1 Pa) and then backfilled with pure oxygen (purity 99.999 vol. %) for three cycles. Oxygen partial pressures (p_{O_2}) at room temperature were p_{O_2} = 0.47 bar, p_{O_2} = 0.45 bar and p_{O_2} = 0.44 bar corresponding to p_{O_2} = 1 bar at 350, 375 and 400 °C, respectively. The sealed quartz tubes were isothermally heated at 350, 375 and 400 °C in a tube furnace (OTF-1200X, Hefei Kejing Materials Technology Co. Ltd.). After the thermal oxidation, the quartz tubes were taken out of the furnace and quenched immediately in water to room temperature.

An Au marker experiment was designed to clarify the atomic transport mechanism during the oxidation of the c-Al_2Zr and am-$Al_{68at.\%}Zr_{32at.\%}$ alloys. To this end, an ultra-thin (thickness ~2 nm) Au film was deposited on the c-Al_2Zr and am-$Al_{68at.\%}Zr_{32at.\%}$ alloys by magnetron sputtering of pure Au (purity 99.999 wt. %) in a high-vacuum sputter system (employing a target power of 10 W for 90 s). The Au-covered c-Al_2Zr and am-$Al_{68at.\%}Zr_{32at.\%}$ alloys were then oxidized at 400 °C for 10 h.

2.3. Analysis and data evaluation

2.3.1. Atomic force microscopy & Optical microscopy (AFM & OM)

AFM operated in tapping mode with a scan frequency of 0.878 Hz was used to measure the surface structure and roughness of the as-polished c-Al_2Zr alloys. The c-Al_2Zr alloys were then corroded (H_2O:HNO_3:HF = 10:1:1 vol ratio) for 3 s and investigated on an Olympus B41 M optical microscope.

2.3.2. X-ray diffraction (XRD)

The as-received and oxidized c-Al_2Zr alloys were investigated by XRD on a Bruker D8 Advanced diffractometer equipped with a Cu X-ray anode (40 kV/40 mA, λ = 1.5418 Å). The diffractometer is in a Bragg-Brentano geometry and the XRD measurements were carried out in a θ-2θ mode. The scanning range of the diffraction angle 2θ was 10–70°, with a step size of 0.02° and a detecting time of 0.15 s/step.

2.3.3. Spectroscopic ellipsometry (SE)

SE (ME-L ellipsomerer, Wuhan Eoptics Technology Co. & J.A. Woollam M-2000) was used to determine the thicknesses of oxide layers on the c-Al_2Zr alloys oxidized at 350 − 400 °C. The ellipsometric values $\Psi(\lambda, \varphi)$ and $\Delta(\lambda, \varphi)$ were recorded from the as-polished and the oxidized c-Al_2Zr alloys over the wavelength of λ = 380 − 1000 nm at incidence angles of φ = 60°, 65° and 70°. Thicknesses of oxide films were determined by linear-least squares (LLS) fitting of $\Psi(\lambda, \varphi)$ and $\Delta(\lambda, \varphi)$ using the WVASE software package (version 3.880). The optical model of the oxide/substrate system used for the fitting constituted three layers of uniform thicknesses, i.e. the c-Al_2Zr alloy substrate, the oxide overlayer (of uniform thickness: L_{ox}) and an interfacial sublayer (of uniform thickness: L_{inter}) between the substrate and the oxide overlayer [29]. The oxide layer is optically transparent over the investigated wavelength range ($k(\lambda) = 0$) and thus the optical constants of the oxide layer were fitted by a Cauchy function $n(\lambda) = A + B/\lambda^2$. The optimized Cauchy constants were A = 1.824, B = 0.02 μm^2 for 350 °C, A = 1.836, B = 0.02 μm^2 for 375 °C, and A = 1.848, B = 0.02 μm^2 for 400 °C, respectively. This corresponds to a refractive index at λ = 632.8 nm of n = 1.874 at 350 °C, n = 1.886 at 375 °C and n = 1.898 at 400 °C, considerably higher than that of α-Al_2O_3 (n = 1.765 [30] and n = 1.772 [31] at λ = 632.8 nm), but lower than that of t-ZrO_2 (n = 2.192 [32] and n = 1.976 [33] at λ = 632.8 nm, and also the optical data in the Ref. [34]) and the oxide film on the am- $Al_{0.44}Zr_{0.56}$ alloy ($2.090 \le n \le 2.119$ [24] at λ = 600 nm). The optical properties of the interfacial sublayer were approximated from the optical properties of the substrate and the oxide overlayer using the Bruggeman effective medium approximation (while taking equal volume percentages for the substrate and the oxide, i.e. 50:50). The total thickness of oxide layer, d_{ox}, was taken as $d_{ox} = L_{ox} + 0.5L_{inter}$.

2.3.4. Auger electron spectroscopy (AES)

The oxidized c-Al_2Zr alloys were investigated by AES sputter-depth profiling in a PHI 700Xi scanning Auger nanoprobe system (base pressure 5 × 10^{-7} Pa), with a field-emission electron gun operated at 5 keV. Sputter-depth profiling was performed with a focused 2 kV Ar^+ beam rastering the surface (sputter rate: 2 nm/min for SiO_2), scanning an area of 100 × 100 μm^2. The spectra of the Al *KLL*, Zr *MNN* and O *KLL* Auger electrons were recorded after each successive sputtering step. The concentration-depth profiles of the oxidic and metallic Al and Zr were obtained by LLS fitting of the corresponding differential AES spectra (MultiPak, v 9.5.0.8). The quantifications of Al and Zr in their metallic (Al^{met} and Zr^{met}) and oxidic (Al^{ox} and Zr^{ox}) states, as well as of O, were carried out according to the procedure described in Ref. [24], while employing the following relative sensitivity factors S (with respect to metallic Zr): $S_{Zr^{met}}$ = 1.000, $S_{Zr^{ox}}$ = 0.627, $S_{Al^{met}}$ = 0.178, $S_{Al^{ox}}$ = 0.411 and S_O = 1.312.

2.3.5. Transmission electron microscopy (TEM)

Cross-sectional TEM lamella were prepared using a so-called 'tripod-polishing method' [35]. The c-Al_2Zr specimen oxidized at 400 °C for 10 h was investigated by TEM in a JEOL JEM-2100 F microscope operated at an acceleration voltage of 200 kV.

2.4. Computational methods

The oxygen diffusivities in the c-Al_2Zr and am-$Al_{68at.\%}Zr_{32at.\%}$ alloys were simulated using the Forcite module in the software Materials Studio (MS) using the universal force field (UFF) [36] including bond order assignment, in which parameter generation is based on physically realistic rules. The c-Al_2Zr alloy was modelled using a $3 \times 3 \times 3$ unit cell (lattice parameters: a = b = 15.843 Å, c = 26.226 Å, $\alpha = \beta = 90°$, and $\gamma = 120°$). To obtain the structural model of the am-$Al_{68at.\%}Zr_{32at.\%}$ alloy, a heating procedure was conducted on the c-Al_2Zr alloy using the temperature cycle protocol in the Forcite module. The NVT [37] ensemble with a Nose thermostat was selected to optimize the equilibration system. The c-Al_2Zr was heated over its melting temperature (4000 K) and then quenched to room temperature at a rate of 1×10^{12} K/s. A final equilibrium step was run for 5 ns. The amorphous configuration of simulated alloy is confirmed based on the radial distribution function (RDF) of the am-$Al_{68at.\%}Zr_{32at.\%}$ alloy [38]. To simulate the oxygen diffusion in the c-Al_2Zr and am-$Al_{68at.\%}Zr_{32at.\%}$ alloy system, respectively, an oxygen atom was introduced into the respective simulation cell with random initial velocities. Geometry optimization was performed for the initial cell with the conjugate gradient (CG) algorithm [39]. The convergence criterions were 1×10^{-4} kcal/mol for energy, 5×10^{-4} kcal/mol/Å for force, 5×10^{-4} GPa for stress, and 5×10^{-5} Å for atomic displacement. After iteration for 500 times, the external pressure was adjusted to 10^{-5} GPa. During the simulation of oxygen diffusion in c-Al_2Zr and am-$Al_{68at.\%}Zr_{32at.\%}$ at 350, 375, and 400 °C, the time-step was set at 1 fs and the total simulation time was maintained at around 10 ns.

3. Results

3.1. Oxide microstructure

The XRD pattern of the as-received c-Al_2Zr specimen confirmed that the alloy was composed of a single-phase intermetallic phase with a hexagonal close-packed (hcp) structure (Fig. 1a). The c-Al_2Zr alloy showed a very large average grain size (> 10 µm, Fig. 1b) and, consequently, the influence of alloy GBs on the oxidation behaviour of the crystalline alloy could be neglected in this case. The surface of c-Al_2Zr after polishing (before oxidation) was very smooth with an average RMS (root-mean-squared) roughness below 1 nm, as determined by AFM (Fig. 1c).

After thermal oxidation of c-Al_2Zr at 350 and 400 °C for 10 h, no additional diffraction peaks could be detected for the alloy and/or oxide by XRD (Fig. 1a). This suggests that the oxide layers formed on the c-Al_2Zr alloys were fully amorphous. The c-Al_2Zr oxidized at 400 °C for 10 h was also investigated by cross-sectional TEM (Fig. 2a; a selected-area diffraction (SAD) pattern taken for the c-Al_2Zr alloy substrate is shown in the inset). TEM analysis confirmed the formation of a homogenous oxide layer of uniform thickness (36 nm) on the surface of c-Al_2Zr. A high-resolution TEM (HRTEM) image of the oxide/c-Al_2Zr interfacial region, marked by the rectangle in Fig. 2a, is shown in Fig. 2b. According to the fast Fourier transform (FFT) of the image in Fig. 2b (inset of Fig. 2b), the oxide layer was also fully amorphous.

The interface between the c-Al_2Zr alloy and the oxide layer was relatively well defined (i.e. not diffuse). Possible enrichment (segregation) of Al or Zr at the alloy/oxide interface could not be detected by analytical TEM (Fig. 3). Corresponding energy-dispersive X-ray spectroscopy (EDX) element mapping of the c-Al_2Zr alloy oxidized at 400 °C for 10 h indicated homogenous distribution of O, Zr and Al in the amorphous oxide layer (Fig. 3). Quantitative EDX analysis of acquired Al *K*, Zr *K*, and O *K* lines suggested a nominal composition of 41 at.% Al, 23at.% Zr, and 36 at.% O for the amorphous oxide layer. The corresponding Al^{3+}/Zr^{4+} atomic ratio in the oxide layer of about 2 agreed well with the respective Al/Zr atomic ratio of 2 for the underlying c-Al_2Zr alloy.

It was concluded that prolonged thermal oxidation of the c-Al_2Zr alloy at 350 and 400 °C resulted in the formation of a chemically homogenous, amorphous Al–Zr–O overlayer of uniform thickness.

3.2. Oxide composition

As evidenced by the obtained AES depth profiles, the amorphous oxide overlayers grown on the c-Al_2Zr alloy (oxidized at 350, 375, and 400 °C for 10 h) had a fixed stoichiometric bulk composition (i.e. in the interior part) of $(Al_{0.68}Zr_{0.32})O_{1.66}$, which was in agreement with the EDX results (Fig. 4a–c). Hence, the average atomic ratio of Al/Zr ($= 2^{\pm 0.1}$) of the oxide overlayer fairly matched that of the c-Al_2Zr substrate. Surprisingly, the oxide overlayers grown on the respective am-$Al_{68at.\%}Zr_{32at.\%}$ alloy at temperatures of 350–400 °C showed a **very different** composition of $(Al_{0.33}Zr_{0.67})O_{1.83}$ (Fig. 4d–f) [14]. This implies that the oxide layers on the am-$Al_{68at.\%}Zr_{32at.\%}$ alloy were much more enriched with Zr compared to the parent alloy substrate (since the Al/Zr atomic ratio of the alloy of 0.5 was much smaller than 2). Interestingly, only the surface region of the oxide layer (up to a sputter depth of about 3 nm) showed the composition $(Al_{0.68}Zr_{0.32})O_{1.66}$,

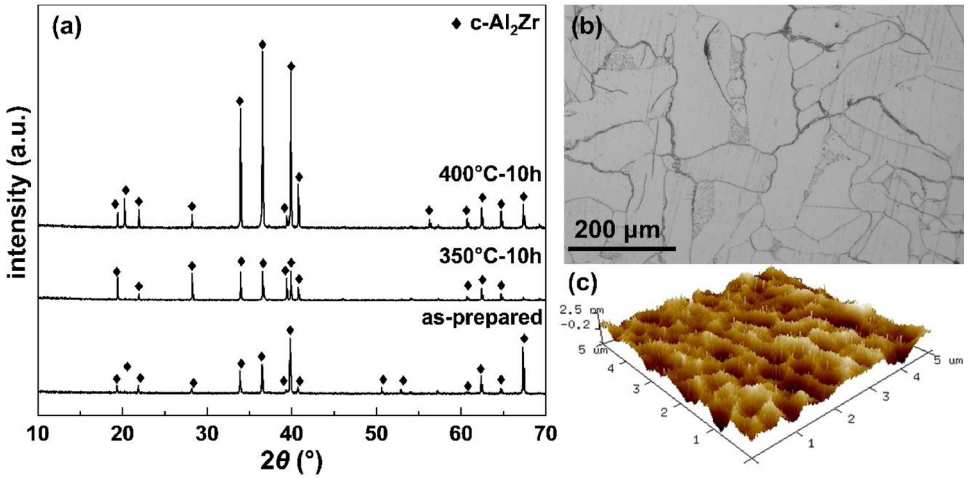

Fig. 1. (a) X-ray diffraction (XRD) patterns and images obtained by (b) optical microscopy (OM) and (c) atomic force microscopy (AFM) for the c-Al_2Zr alloy.

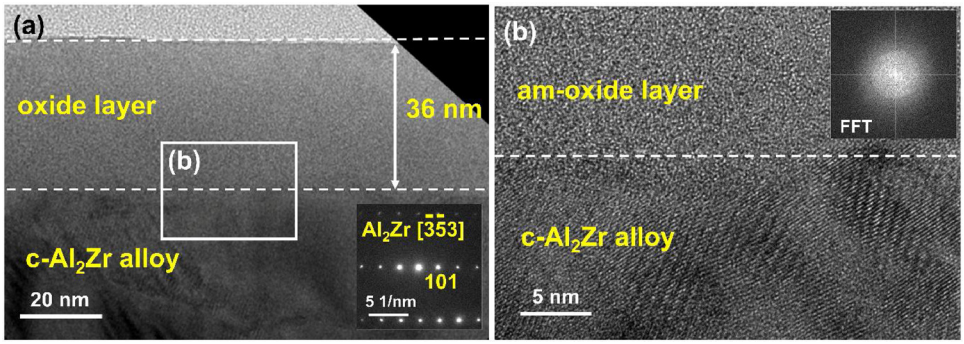

Fig. 2. (a) Cross-sectional transmission electron microscopy (TEM) image obtained for c-Al_2Zr alloy oxidized at 400 °C for 10 h, with the selected-area diffraction pattern of c-Al_2Zr alloy shown in the inset, and (b) high-resolution TEM image of the oxide/c-Al_2Zr interfacial region marked by the rectangle in (a) and fast Fourier transform obtained exclusively within the oxide region.

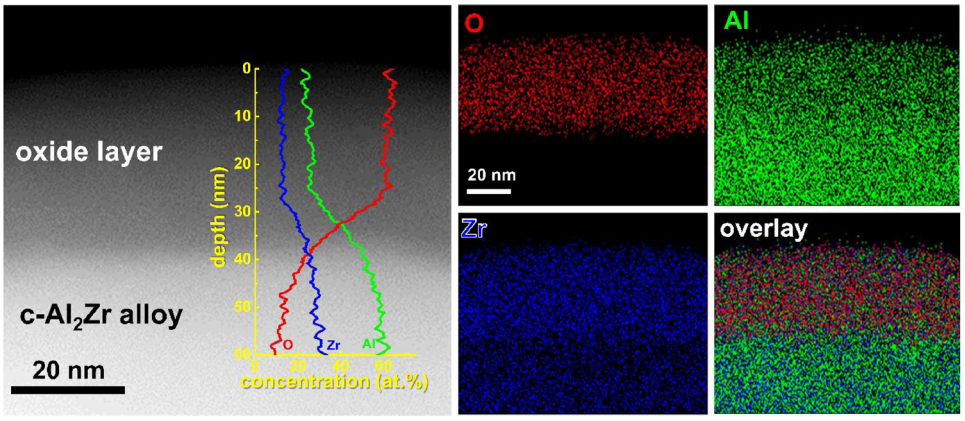

Fig. 3. Energy-dispersive X-ray spectroscopy (EDX) element line scan and mapping results for the c-Al_2Zr alloy oxidized at 400 °C for 10 h.

corresponding to the expected Al^{ox}/Zr^{ox} ratio of ~2 (i.e. matching that of the alloy surface), as shown in Fig. 4d–f. The surface region showing a deviating composition can likely be rationalised by the original passive oxide layer, which formed spontaneously on the polished am-$Al_{68at.\%}Zr_{32at.\%}$ surface upon exposure to ambient conditions. Within the studied oxidation temperature range, extensive dissolution and inward diffusion of oxygen into the c-Al_2Zr and am-$Al_{68at.\%}Zr_{32at.\%}$ [14] substrates did not occur owing to the relatively higher content of Al [38] (Fig. 4).

Au marker experiments were conducted for the oxidation of c-Al_2Zr and am-$Al_{68at.\%}Zr_{32at.\%}$ at 400 °C for 10 h by AES depth profiling (Fig. 5). For both alloys, the pre-deposited ultra-thin (nominal thickness: ~2 nm) inert Au markers remained on the outer oxide surface instead of being buried in the thickening oxide layer. This suggests that oxide layer growth occurred mainly at the interface between the developing oxide layer and the parent alloy through inward diffusion of oxygen anions (with concurrent outward diffusion of anion vacancies, which were generated at the oxide/alloy interface by continuous dissolution of O into the alloy), in accordance with the oxidation mechanism for pure Zr metal as proposed previously [40,41].

3.3. Oxidation kinetics

The oxide layer growth curves demonstrating the growth of the amorphous oxide layers on am-$Al_{68at.\%}Zr_{32at.\%}$ and c-Al_2Zr alloys at 350–400 °C were determined by SE, as shown in Fig. 6a and b, respectively. The layer thicknesses determined by SE agreed well with those determined by TEM.

The oxidation kinetics of the c-Al_2Zr alloy was seen to follow **a linear rate law** (Fig. 6b) according to the following equation:

$$d(t) = K_l t + d_0(T) \quad (1)$$

where d is the oxide layer thickness, t is the oxidation time, K_l is the linear growth rate constant, and $d_0(T)$ is introduced here to account for the combined effects of the native oxide and an initial, very fast oxidation stage (before the formation of a laterally-closed oxide layer at the alloy surface) [26,42]. The linear oxide growth indicated that the oxidation rate was limited by the reaction steps at the oxide surface or the alloy/oxide interface, presumably either the dissociative chemisorption of oxygen molecules at the oxide surface or the dissolution of oxygen from the oxide into the parent alloy at the alloy/oxide interface, respectively. The experimentally determined K_l values were 2.4×10^{-13}, 3.9×10^{-13}, and 6.6×10^{-13} m/s at 350, 375, and 400 °C, respectively.

On the contrary, the oxidation kinetics of am-$Al_{68at.\%}Zr_{32at.\%}$ did not follow a linear growth law, but instead followed **a parabolic rate law** [29], characteristic for a diffusion rate-limited process, according to the following equation:

$$d(t) = \sqrt{2K_p t + d_0(T)^2} \quad (2)$$

where K_p is the parabolic growth-rate constant. Notably, the linear oxidation rate of the c-Al_2Zr alloy was, on average, **much higher** than the (parabolic) oxidation rate of am-$Al_{68at.\%}Zr_{32at.\%}$ alloy at the same temperature (Fig. 6), i.e. d(c-Al_2Zr) > > d(am-$Al_{68at.\%}Zr_{32at.\%}$), as shown in Table 1. The temperature dependence of the linear and parabolic growth rate constants should typically follow an Arrhenius temperature dependence [43], according to the equation

$$K(T) = K_0 \exp(-\frac{Q}{R \cdot T}) \quad (3)$$

where K_0 is a pre-exponential factor, Q is the effective activation energy of the rate-limiting reaction step(s), R is the gas constant, and T is the oxidation temperature. The effective activation energy, Q, pertaining to the rate-limiting reaction step(s) of the oxidation process, could be determined by least-squares fitting of the series of growth curves of each alloy over the studied oxidation temperatures (Table 1). In the rate-controlling step of the oxidation process, the values of Q were similar for c-Al_2Zr (Q = 70 kJ/mol = 0.73 eV) and am-$Al_{68at.\%}Zr_{32at.\%}$

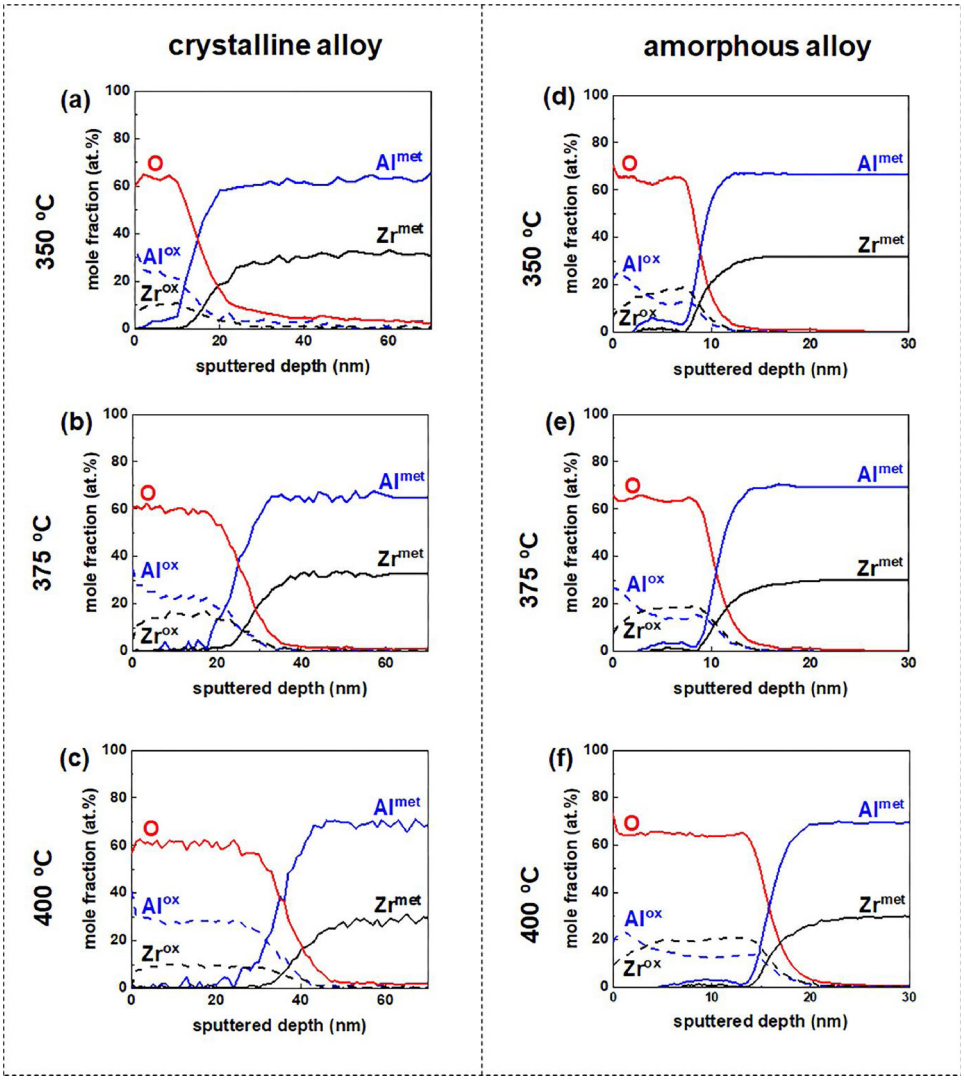

Fig. 4. Auger electron spectroscopy (AES) depth profiles for c-Al_2Zr alloys oxidized at (a) 350 °C, (b) 375 °C, and (c) 400 °C for 10 h, and am-$Al_{68at.\%}Zr_{32at.\%}$ alloys oxidized at (d) 350 °C, (e) 375 °C, and (f) 400 °C for 10 h.

(Q = 73 kJ/mol = 0.76 eV), even though their oxidation rates were distinctly different.

4. Discussion

4.1. Developing oxide microstructure

An ultrathin (thickness < 5 nm) passive oxide film spontaneously formed on c-Al_2Zr and am-$Al_{68at.\%}Zr_{32at.\%}$ upon exposure of the as-prepared alloy surfaces to the ambient atmosphere (prior to oxidation). The initial oxidation associated with the formation of the passive oxide is extremely fast, while atomic mobility in the alloy substrate at room temperature is practically negligible. Then, since Al and Zr show similar oxygen affinities, oxygen in the air reacts spontaneously with Zr and Al at the alloy (sub)surface to form an oxide with the same Zr/Al ratio (= 2) as the parent c-Al_2Zr and am-$Al_{68at.\%}Zr_{32at.\%}$ substrates, as observed in the present study.

The native oxide films formed on the c-Al_2Zr and am-$Al_{68at.\%}Zr_{32at.\%}$ surfaces are predominantly amorphous, which is thermodynamically preferred due to the relatively low surface and interface energies of the amorphous oxide state (compared to those of the corresponding crystalline oxide state) [44,45]. On the contrary, the amorphous state of the thermally grown oxide layers (thicknesses: 7–37 nm) on both alloys at 350–400 °C is only metastable; the transformation from amorphous to crystalline state, with a lower (bulk) energy, is kinetically hindered at these intermediate temperatures owing to the large nucleation barrier for crystallization. The decomposition and crystallization of the amorphous (Zr,Al,O) oxides into their competing crystalline Al_2O_3 and/or ZrO_2 phases (note that crystalline Al_2O_3 and crystalline ZrO_2 are not mutually soluble) requires sufficient atomic mobility in the oxide to form stable nuclei of the competing crystalline oxide phases. In addition, phase separation of the amorphous ternary oxide into two new crystalline phases will involve energy penalties associated with (*i*) the creation of new interfaces between the product phase and its surrounding matrix ($\Delta G_{interface}$), as well as (*ii*) the generation of elastic strain energy due to the huge volume mismatch between the parent and product phases (ΔG_{strain}). Consequently, relatively high temperatures are required to crystallize the amorphous (Zr,Al) oxide phases (e.g. about $T > 800$ K for amorphous (Zr,Al)-oxide layers on am-$Al_{68at.\%}Zr_{32at.\%}$) [24].

4.2. Oxidation mechanism

The c-Al_2Zr and am-$Al_{68at.\%}Zr_{32at.\%}$ have practically identical chemical compositions but exhibit distinct differences in their oxidation behaviours, which highlights the vital role of structural order in the

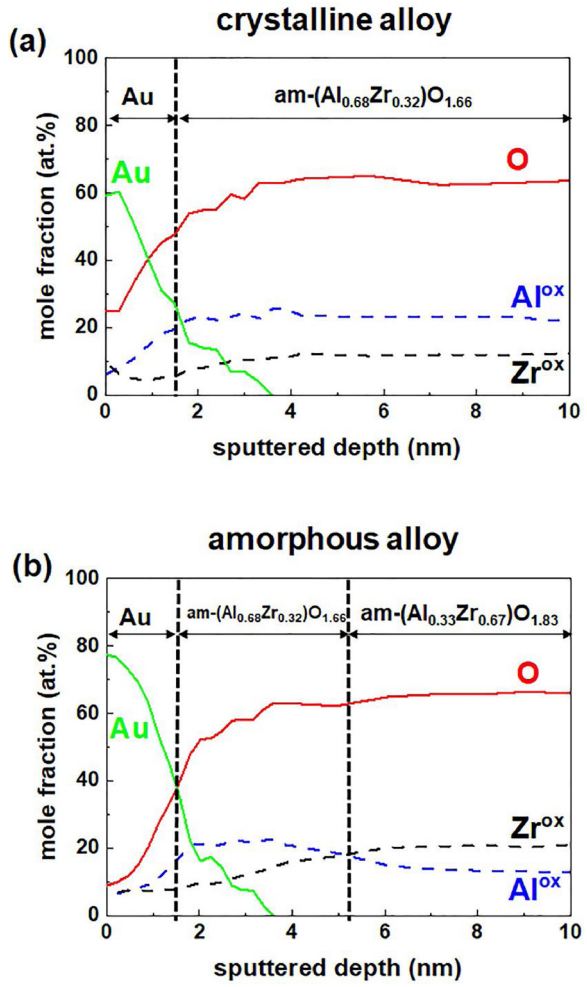

Fig. 5. Auger electron spectroscopy (AES) depth profiles for Au-labelled (a) c-Al_2Zr and (b) am-$Al_{68at.\%}Zr_{32at.\%}$ alloys oxidized at 400 °C for 10 h.

parent alloy in determining the oxidation mechanism. Thermal oxidation of c-Al_2Zr and am-$Al_{68at.\%}Zr_{32at.\%}$ not only resulted in different growth rates, but also led to distinctly different compositions of the amorphous oxide overlayers: i.e. $(Al_{0.68}Zr_{0.32})O_{1.66}$ and $(Al_{0.33}Zr_{0.67})O_{1.83}$ for the oxidation of c-Al_2Zr and am-$Al_{68at.\%}Zr_{32at.\%}$ alloy, respectively.

As indicated by the Au marker experiments, growth of the amorphous oxide layers on both alloys proceeds by inward diffusion of oxygen with the formation of new oxide species at the oxide/alloy interface. Previous diffusion marker studies undertaken by Kai *et al.* [46], $^{18}O_2$ isotopic tracer experiments conducted by Wang et al. [47] on Zr-based metallic glasses, as well as a study by Prescott [40] on the oxidation of Al-based alloys confirmed oxygen diffusion-controlled oxidation of both Zr-based and Al-based alloys for the studied composition range.

The following processes can be rate-limiting for the oxidation of the crystalline Al_2Zr and amorphous $Al_{68at.\%}Zr_{32at.\%}$ alloys in the studied temperature range of 350–400 °C [41]:

(i) O vacancy diffusion in the oxide lattice (resulting in a parabolic rate)
(ii) a surface (sub)reaction at the O_2(g)/oxide interface (e.g. dissociative chemisorption or filling of O vacancies at the gas/oxide interface)
(iii) injection of O vacancies in the growing oxide layer by dissolution of oxygen into the alloy substrate at the oxide/alloy interface

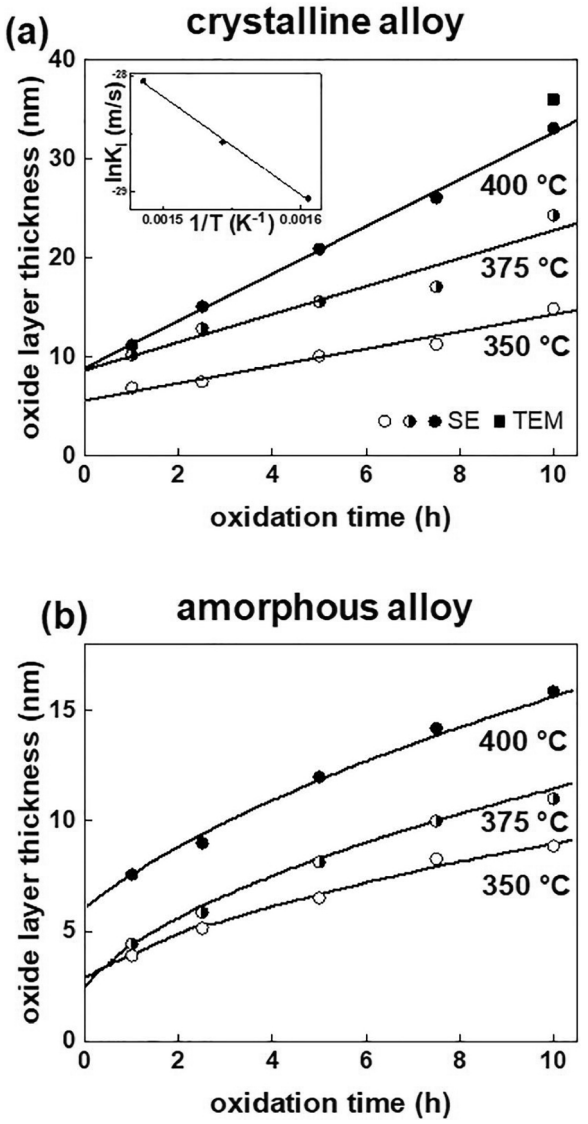

Fig. 6. Thicknesses of oxide layers on (a) c-Al_2Zr alloy ($\ln K_l$ for oxidation of c-Al_2Zr alloy as a function of 1/T shown in the inset) and (b) am-$Al_{68at.\%}Zr_{32at.\%}$ alloy as a function of oxidation time at the temperatures of 350–400 °C.

Table 1
Oxide layer growth parameters for c-Al_2Zr and am-$Al_{68at.\%}Zr_{32at.\%}$ alloys [29]: activation energy Q and oxide layer thickness d at t = 10 h.

Specimen	Mode	Q (kJ/mol)	d for 10 h (nm)		
			350 °C	375 °C	400 °C
c-Al_2Zr	linear	70	14.9	24.3	33.1
am-$Al_{68at.\%}Zr_{32at.\%}$ [29]	parabolic	73	8.9	11.0	15.9

Ad (i): The chemical diffusion coefficient of oxygen in bulk ZrO_2 is typically much higher than that in bulk Al_2O_3 (3.2×10^{-8} m^2/s for ZrO_2 at 1000 °C [48] and 2.7×10^{-14} m^2/s for Al_2O_3 at 1000 °C [49]). It might then be naively assumed that oxygen diffusion and thus the oxidation rate in the amorphous (Al,Zr) oxide would be higher for a lower Al concentration in the mixed (Al,Zr) oxide phase (i.e. a lower Al^{ox}/Zr^{ox} ratio), provided the molar density of oxygen in the oxide remains approximately constant. The molar densities of oxygen, D_O, in the am-$(Al_{0.33}Zr_{0.67})O_{1.83}$ and am-$(Al_{0.68}Zr_{0.32})O_{1.66}$ overlayers were estimated from the corresponding molar densities of amorphous Al_2O_3 [50] and ZrO_2 [51] assuming average compositions of

Table 2
Mass densities of materials investigated and molar oxygen densities of corresponding amorphous oxides [50,51].

Material	Mass Density (g/cm^3)	Atomic Density D_O (10^4 mol/m^3)
am-Al_2O_3	3.175 [50]	9.342
am-ZrO_2	5.537 [51]	8.986
am-$(Al_{0.33}Zr_{0.67})O_{1.83}$	4.758	9.103
am-$(Al_{0.68}Zr_{0.32})O_{1.66}$	3.931	9.228

$(AlO_{1.5})_{0.33}(ZrO_2)_{0.67}$ and $(AlO_{1.5})_{0.68}(ZrO_2)_{0.32}$, respectively (Table 2). The estimated oxygen molar densities observed for am-$(Al_{0.68}Zr_{0.32})O_{1.66}$ oxide on c-Zr_2Al and am-$(Al_{0.33}Zr_{0.67})O_{1.83}$ oxide on am-$Al_{68at.\%}Zr_{32at.\%}$ were 9.103×10^4 and 9.228×10^4 mol/m^3, respectively, which are very similar. This suggests that the oxygen chemical diffusion coefficient in the Al-enriched am-$(Al_{0.68}Zr_{0.32})O_{1.66}$ oxide (with Al^{ox}/Zr^{ox} ratio = 2) on the c-Al_2Zr alloy should be lower than that in the Zr-enriched am-$(Al_{0.33}Zr_{0.67})O_{1.83}$ oxide (with Al^{ox}/Zr^{ox} ratio = 0.5) on the am-$Al_{68at.\%}Zr_{32at.\%}$ alloy. However, the opposite is observed in the present study (i.e. the oxidation rate is much faster for the c-Al_2Zr alloy with the Al-rich oxide overlayer): see Fig. 6. Moreover, the oxidation kinetics for the c-Al_2Zr alloy follow **a linear growth law**, whereas a parabolic growth law would be expected for oxygen diffusion-controlled growth. Hence the hypothesis that the oxidation of both alloys is rate-limited by the chemical diffusion of oxygen in the oxide can be ruled out.

Ad (ii): If the oxidation would be rate-limited by a reaction rate at the oxide surface (e.g. dissociative chemical adsorption), the growth kinetics of the amorphous oxide overlayer would proceed at a similar, linear rate for both alloys, since the surface compositions of the oxide layers are practically identically (as determined by the stage of passive oxide film formation prior to thermal oxidation: see Section 4.1). This is not the case in this work.

Ad (iii): Oxygen lattice transport through the thickening oxide layers requires coupled fluxes of inwardly migrating oxygen anions and outwardly migrating O vacancies (as coupled to diffusion fluxes of electrons and electron holes). In this case, O vacancies are generated by oxygen dissolution at the alloy/oxide interface and are subsequently injected into the growing oxide layer. The dissolved oxygen in the alloy may diffuse from the alloy/oxide interface into the interior of the parent alloy and/or locally reach a critical concentration to nucleate an oxide. Such oxygen dissolution and, particularly, oxygen inward diffusion will be affected by the atomic arrangement in the parent alloy. For example, as demonstrated by Bakradze *et al.* [42], for single-crystalline α-Zr, the less densely packed Zr(10$\bar{1}$0) surface oxidizes more rapidly than the densely packed Zr(0001) surface, which can be attributed to the anisotropy of the oxygen diffusion coefficient in the hcp structure (the oxygen diffusivities are $D_{basal} = 2.4 \times 10^{-21}$ m^2/s and $D_{prism} = 4.8 \times 10^{-21}$ m^2/s for α-Zr at $T = 450$ K, respectively).

The diffusivities of oxygen in the c-Al_2Zr and am-$Al_{68at.\%}Zr_{32at.\%}$ alloys were estimated by MD simulations. The diffusion coefficient D was determined as follows: [52]

$$D = \frac{<R^2(t)>}{6t} \quad (5)$$

where $< R^2(t) >$ is the mean square displacement (MSD) of diffusing atoms and t is the simulation time. Derived from the slopes of the fitted line of MSD against t (Fig. 7), the ratios of diffusivities of oxygen in the c-Al_2Zr and am-$Al_{68at.\%}Zr_{32at.\%}$ alloys, $\frac{D_{O\text{ in c-}Al_2Zr}}{D_{O\text{ in am-}Al_{68at.\%}Zr_{32at.\%}}}$, were 1.44 at 350 °C, 1.64 at 375 °C, and 1.16 at 400 °C, respectively, which indeed confirms that oxygen diffuses faster in c-Al_2Zr than in am-$Al_{68at.\%}Zr_{32at.\%}$. Ordered interstitial sites are only present in the c-Al_2Zr alloy (and are absent in the am-$Al_{68at.\%}Zr_{32at.\%}$ alloy); these ordered interstitial sites enable fast oxygen migration in the crystalline alloy matrix, which in turn results in a relatively high injection rate of O

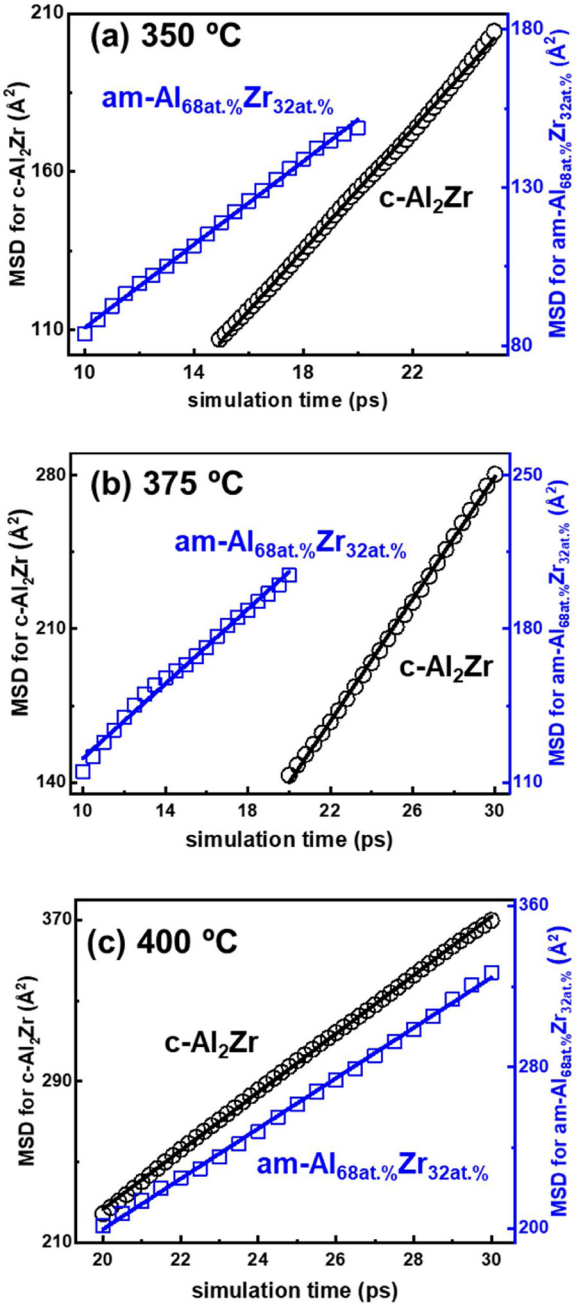

Fig. 7. Mean square displacements (MSD) for c-Al_2Zr and am-$Al_{68at.\%}Zr_{32at.\%}$ alloys at (a) 350 °C, (b) 375 °C, and (c) 400 °C.

vacancies in the developing oxide at the reaction front (i.e. the alloy/oxide interface). Due to the absence of long-range order, am-$Al_{68at.\%}Zr_{32at.\%}$ does not provide any well-defined, energetically-favourable interstitial sites pathways for inward diffusion of O (as is the case for c-Al_2Zr). Consequently, the rate of oxygen dissolution and therefore the injection rate of oxygen vacancies into the growing layer are suppressed, resulting in the observed decrease in the oxidation rate for am-$Al_{68at.\%}Zr_{32at.\%}$. It may thus be assumed that the disordered atomic arrangement in am-$Al_{68at.\%}Zr_{32at.\%}$ retards not only the oxygen dissolution at the alloy/oxide interface, but also the subsequent inward diffusion of dissolved oxygen into am-$Al_{68at.\%}Zr_{32at.\%}$. As such, the generation of available sites for oxygen dissolution into am-$Al_{68at.\%}Zr_{32at.\%}$ is partially blocked by the retarded inward diffusion rate of oxygen into am-$Al_{68at.\%}Zr_{32at.\%}$, which would also explain the observed parabolic oxidation kinetics (characteristic for a diffusion-

controlled reaction rate) see also Section 3.3.

4.3. Developing oxide composition

The am-$(Al_{0.33}Zr_{0.67})O_{1.83}$ phase with a Al^{3+}/Zr^{4+} ratio of about 0.5, which formed on the oxidized am-$Al_{68at.\%}Zr_{32at.\%}$ alloy, corresponds to the lowest Gibbs energy of formation, ΔG, for the Al_2O_3–ZrO_2 pseudo binary system (i.e. the lowest enthalpy of mixing of am-Al_2O_3 and am-ZrO_2) and is thus thermodynamically preferred, as discussed in detail previously [14]. The oxide layer formed on c-Al_2Zr is also amorphous, but shows a very different composition of am-$(Al_{0.68}Zr_{0.32})O_{1.66}$, corresponding to an Al^{3+}/Zr^{4+} ratio of about 2, which is the same as that of the c-Al_2Zr substrate. The am-$(Al_{0.68}Zr_{0.32})O_{1.66}$ layer can be formed on the c-Al_2Zr alloy at temperatures as high as 750 °C [53]. The question arises if the formation of the am-$(Al_{0.68}Zr_{0.32})O_{1.66}$ phase on the c-Al_2Zr alloy can also be rationalized on the basis of thermodynamics or if it has a kinetic origin.

As discussed in Section 4.2, it may be assumed that oxygen diffusion through interstitial sites into the ordered hexagonal lattice of c-Al_2Zr is much faster than oxygen diffusion in the disordered atomic arrangement of am-$Al_{68at.\%}Zr_{32at.\%}$. This implies that oxygen can easily diffuse to and distribute between energetically favourable interstices in the c-Al_2Zr lattice to form an amorphous (Al,Zr) oxide phase with a stoichiometric Al/Zr ratio, which is equivalent to that of the original c-Al_2Zr unit cell (i.e. Al/Zr = 2). Hence, no substantial diffusion or exchange of Al and Zr atoms in the c-Al_2Zr lattice is necessary for continuing the oxide layer growth. Due to the fast diffusion of oxygen and relative immobilization of the Al and Zr atoms in the crystal lattices, the Al^{3+}/Zr^{4+} ratio in the oxide layer formed on the Al_2Zr alloy was almost the same as that of the substrate. As indicated by the Arrhenius analysis of the oxidation kinetics in Section 3.3, the rate-limiting step of the oxidation process was the dissolution of oxygen into c-Al_2Zr at the migrating reaction front (i.e. the oxide/alloy interface) and not the diffusion of oxygen in c-Al_2Zr.

As discussed in Section 4.2, both oxygen dissolution and oxygen diffusion are hindered by the absence of long-range order in am-$Al_{68at.\%}Zr_{32at.\%}$. Consequently, the formation of a compositionally homogenous region in am-$Al_{68at.\%}Zr_{32at.\%}$ (i.e. with a constant elemental distribution of Al, Zr, and O on a local scale) not only requires a certain atomic mobility of oxygen in the alloy, but also necessitates specific atomic arrangements of Al and Zr (*note:* the mobility of Al in the alloy is likely higher than that of Zr [29]). Consequently, the rate of oxide formation in the am-$Al_{68at.\%}Zr_{32at.\%}$ alloy is significantly suppressed in comparison with that in the c-Al_2Zr alloy. Local redistribution of O, Al, and Zr (i.e. local chemical fluctuations) are required to form a stable critical nucleus size for the thermodynamically preferred am-$(Al_{0.33}Zr_{0.67})O_{1.83}$ phase with a Al^{3+}/Zr^{4+} ratio of about 0.5 [14]. Consequently, parabolic oxidation kinetics could be observed (Section 3.3), which is characteristic of a diffusion-controlled oxidation process.

5. Conclusions

- The oxidation of amorphous and crystalline Al–Zr binary alloys has been investigated on a comparative basis to disclose the effect of structural order on the underlying oxidation mechanism of metallic alloys.
- An amorphous oxide phase with a well-defined stoichiometric composition of $(Al_{0.68}Zr_{0.32})O_{1.66}$ formed on the crystalline Al_2Zr alloy at 350–400 °C, in striking contrast with the formation of an $(Al_{0.33}Zr_{0.67})O_{1.83}$ amorphous oxide on the amorphous $Al_{68at.\%}Zr_{32at.\%}$ alloy. The oxidation kinetics of crystalline Al_2Zr alloy was fast and linear, distinctively different from the slow, parabolic oxidation kinetics of the amorphous $Al_{68at.\%}Zr_{32at.\%}$ alloy.
- Based on molecular dynamics simulations, the pronounced role of structural (dis)order of the parent alloy in determining the oxidation behaviour has been disclosed. In the crystalline Al_2Zr alloy, rapid oxygen diffusion along the diffusion path composed of energetically favourable interstitial sites results in fast oxidation kinetics due to the increased rate of injection of O vacancies in the developing oxide at the alloy/oxide interface. On the contrary, oxygen dissolution and diffusion are impeded by the long-range disorder in the amorphous counterpart, resulting in significantly lowered oxidation kinetics.
- The oxide composition on the crystalline Al_2Zr alloy is dictated by kinetics: due to the fast diffusion of oxygen and relative immobilization of Al and Zr atoms in the crystal lattices, the Al^{3+}/Zr^{4+} ratio (≈ 2) in the oxide layer formed on the Al_2Zr alloy is practically the same as that in the substrate. On the contrary, the oxide composition of the amorphous alloy is thermodynamically controlled: oxygen dissolution and inward diffusion in the amorphous alloy are retarded by the structural disorder. The required sluggish re-arrangements of Al and Zr atoms result in a thermodynamically preferred oxide composition of $(Al_{0.33}Zr_{0.67})O_{1.83}$ ($Al^{3+}/Zr^{4+} \approx 0.5$).
- The above findings provide compelling evidences on the intrinsic role of structural order of parent alloys in governing the oxidation kinetics and the evolving oxide phase composition, thus offering a new perspective in the field of surface engineering.

Data availability statement

All data included in this study are available upon request by contact with the corresponding author.

CRediT authorship contribution statement

Yifei Xu: Investigation, Visualization, Writing - original draft. **Lars P.H. Jeurgens:** Conceptualization, Writing - review & editing. **Yuan Huang:** Software. **Chong Li:** Resources. **Yongchang Liu:** Project administration. **Zumin Wang:** Conceptualization, Writing - review & editing, Project administration, Funding acquisition.

Declaration of Competing Interest

The authors declare that they have no known competing financial interests or personal relationships that could have appeared to influence the work reported in this paper.

Acknowledgements

This work was supported by the National Natural Science Foundation of China (No. 51571148) and the National Key Research and Development Program of China (No. 2017YFE0302600 and No. 2017YFB0701801).

References

[1] H. Over, A.P. Seitsonen, Oxidation of metal surfaces, Science 297 (2002) 2003–2005.
[2] N. Birks, G.H. Meier, F.S. Pettit, Introduction to the High Temperature Oxidation of Metals, Cambridge University Press, Cambridge, 2006.
[3] K. Takada, H. Sakurai, E. Takayama-Muromachi, F. Izumi, R.A. Dilanian, T. Sasaki, Superconductivity in two-dimensional CoO_2 layers, Nature 422 (2003) 53–55.
[4] K.Y. Frolenkov, L.Y. Frolenkova, I.F. Shadrin, High-temperature oxidation of low-alloyed steel under glass coatings, Prot. Met. Phys. Chem. Surf. 46 (2010) 103–109.
[5] J.S. Park, W.J. Maeng, H.S. Kim, J.S. Park, Review of recent developments in amorphous oxide semiconductor thin-film transistor devices, Thin Solid Films 520 (2012) 1679–1693.
[6] P. Huczkowski, S.G. Gopalakrishnan, W. Nowak, H. Hattendorf, R. Iskandar, J. Mayer, W.J. Quadakkers, Effect of Zr content on the morphology and emissivity of surface oxide scales on FeCrAlY alloys adv, Eng. Mater. 18 (2016) 711–720.
[7] T. Huang, D. Naumenko, P. Song, J. Lu, W.J. Quadakkers, Effect of titanium addition on alumina growth mechanism on yttria-containing FeCrAl-base alloy, Oxid. Met. 90 (2018) 671–690.
[8] L. Boatemaa, M. Bosch, A.S. Farle, G.P. Bei, S. van der Zwaag, W.G. Sloof, Autonomous high-temperature healing of surface cracks in Al_2O_3 containing Ti_2AlC particles, J. Am. Ceram. Soc. 101 (2018) 5684–5693.

[9] L.P.H. Jeurgens, W.G. Sloof, F.D. Tichelaar, E.J. Mittemeijer, Thermodynamic stability of amorphous oxide films on metals: application to aluminum oxide films on aluminum substrates, Phys. Rev. B 62 (2000) 4707–4719.

[10] F. Reichel, L.P.H. Jeurgens, E.J. Mittemeijer, Thermodynamic model of oxide overgrowth on bare metals: relaxation of growth strain by plastic deformation, Phys. Rev. B 74 (2006).

[11] F. Reichel, L.P.H. Jeurgens, G. Richter, P.A. van Aken, E.J. Mittemeijer, The origin of high-mismatch orientation relationships for ultra-thin oxide overgrowths, Acta Mater. 55 (2007) 6027–6037.

[12] F. Reichel, L.P.H. Jeurgens, E.J. Mittemeijer, The thermodynamic stability of amorphous oxide overgrowths on metals, Acta Mater. 56 (2008) 659–674.

[13] E. Panda, L.P.H. Jeurgens, E.J. Mittemeijer, Interface thermodynamics of ultra-thin, amorphous oxide overgrowths on AlMg alloys, Acta Mater. 58 (2010) 1770–1781.

[14] K. Weller, Z.M. Wang, L.P.H. Jeurgens, E.J. Mittemeijer, Thermodynamics controls amorphous oxide formation: exclusive formation of a stoichiometric amorphous $(Al_{0.33}Zr_{0.67})O_{1.83}$ phase upon thermal oxidation of Al–Zr, Acta Mater. 94 (2015) 134–142.

[15] Z. Xu, Y. Xu, A. Zhang, J. Wang, Z. Wang, Oxidation of amorphous alloys, J. Mater. Sci. Technol. 34 (2018) 1977–2005.

[16] Y. Xu, L.P.H. Jeurgens, P. Schützendübe, S. Zhu, Y. Huang, Y. Liu, Z. Wang, Effect of atomic structure on preferential oxidation of alloys: amorphous versus crystalline Cu-Zr, J. Mater. Sci. Technol. (2020), https://doi.org/10.1016/j.jmst.2019.10.001.

[17] P. Thurnheer, F. Haag, J.F. Löffler, Time-resolved measurement of shear-band temperature during serrated flow in a Zr-based metallic glass, Acta Mater. 115 (2016) 468–474.

[18] K.J. Laws, D. Granata, J.F. Löffler, Alloy design strategies for sustained ductility in Mg-based amorphous alloys – tackling structural relaxation, Acta Mater. 103 (2016) 735–745.

[19] D. Flötotto, Z.M. Wang, L.P.H. Jeurgens, E.J. Mittemeijer, Intrinsic stress evolution during amorphous oxide film growth on Al surfaces, Appl. Phys. Lett. 104 (2014) 091901.

[20] J. Qiao, H. Jia, P.K. Liaw, Metallic glass matrix composites, Mater. Sci. Eng. R Rep. 100 (2016) 1–69.

[21] K. Weller, T. Suter, Z.M. Wang, L.P.H. Jeurgens, E.J. Mittemeijer, The effect of pre-oxidation treatment on the corrosion behavior of amorphous $Al_{1-x}Zr_x$ solid-solution alloys, Electrochim. Acta 188 (2016) 31–39.

[22] Y.S. Jung, J.Y. Seo, D.W. Lee, D.Y. Jeon, Influence of DC magnetron sputtering parameters on the properties of amorphous indium zinc oxide thin film, Thin Solid Films 445 (2003) 63–71.

[23] L. Zeng, D.T. Tran, C.-W. Tai, G. Svensson, E. Olsson, Atomic structure of the ultrathin amorphous aluminium oxide barrier in $Al/AlO_x/Al$ Josephson junctions, European Microscopy Congress 2016: Proceedings (2016).

[24] K. Weller, L.P.H. Jeurgens, Z. Wang, E.J. Mittemeijer, Thermal oxidation of amorphous $Al_{0.44}Zr_{0.56}$ alloys, Acta Mater. 87 (2015) 187–200.

[25] L. Jastrow, U. Köster, Oxidation of Amorphous $Zr_{70}Pd_{30}$ and Coarse Crystalline Zr_2Pd, MRS Proceedings 806 (2004), pp. MM10.61–MM10.66.

[26] T.J. Nijdam, L.P.H. Jeurgens, W.G. Sloof, Effect of partial oxygen pressure on the initial stages of high-temperature oxidation of γ-NiCrAl alloys, Mater. High Temp. 20 (2003) 311–318.

[27] A. Szekeres, P. Danesh, Oxidation of amorphous and crystalline silicon, J. Non. Solids 187 (1995) 45–48.

[28] M. Miyasaka, W. Itoh, H. Ohshima, T. Shimoda, Dry thermal oxidation of polycrystalline and amorphous silicon films for application to thin film transistors, Jpn. J. Appl. Phys. Part 1-Regul. Pap. Short Notes Rev. Pap. 37 (1998) 1076–1081.

[29] K. Weller, Z.M. Wang, L.P.H. Jeurgens, E.J. Mittemeijer, Oxidation kinetics of amorphous Al_xZr_{1-x} alloys, Acta Mater. 103 (2016) 311–321.

[30] H. Yao, C.H. Yan, Anisotropic optical responses of sapphire (α-Al_2O_3) single crystals, J. Appl. Phys. 85 (1999) 6717–6722.

[31] P. Petrik, T. Gumprecht, A. Nutsch, G. Roeder, M. Lemberger, G. Juhasz, O. Polgar, C. Major, P. Kozma, M. Janosov, B. Fodor, E. Agocs, M. Fried, Comparative measurements on atomic layer deposited Al_2O_3 thin films using ex situ table top and mapping ellipsometry, as well as X-ray and VUV reflectometry, Thin Solid Films 541 (2013) 131–135.

[32] R.H. French, S.J. Glass, F.S. Ohuchi, Y.N. Xu, W.Y. Ching, Experimental and theoretical determination of the electronic structure and optical properties of three phases of ZrO_2, Phys. Rev. B 49 (1994) 5133–5142.

[33] A. Lyapin, L.P.H. Jeurgens, P.C.J. Graat, E.J. Mittemeijer, Ellipsometric and XPS study of the initial oxidation of zirconium at room temperature, Surf. Interface Anal. 36 (2004) 989–992.

[34] P. Petrik, A. Sulyok, T. Novotny, E. Perez-Feró, B. Kalas, E. Agocs, T. Lohner, D. Lehninger, L. Khomenkova, R. Nagy, J. Heitmann, M. Menyhard, Z. Hózer, Optical properties of Zr and ZrO_2, Appl. Surf. Sci. 421 (2017) 744–747.

[35] J. Ayache, L. Beaunier, J. Boumendil, G. Ehret, D. Laub, Sample Preparation Handbook for TEM, Springer, Berlin, 2010.

[36] A.K. Rappe, C.J. Casewit, K.S. Colwell, W.A. Goddard, W.M. Skiff, UFF, a full periodic table force field for molecular mechanics and molecular dynamics simulations, J. Am. Chem. Soc. 114 (1992) 10024–10035.

[37] S. Luo, J. Hao, Y. Gao, D. Liu, Q. Cai, X. Yang, Pore size effect on adsorption and release of metoprolol tartrate in mesoporous silica: experimental and molecular simulation studies, Mater. Sci. Eng. C 100 (2019) 789–797.

[38] K. Weller, N. Zotov, Z.M. Wang, L.P.H. Jeurgens, E.J. Mittemeijer, Atomic structure, electronic structure and thermal stability of amorphous Al_xZr_{1-x} ($0.26 \leq x \leq 0.75$), J. Non. Solids 427 (2015) 104–113.

[39] J.E. Dennis, R.B. Schnabel, Chapter I A view of unconstrained optimization, Handbooks in Operations Research and Management Science, Elsevier, 1989, pp. 1–72.

[40] R. Prescott, M.J. Graham, The formation of aluminum oxide scales on high-temperature alloys, Oxid. Met. 38 (1992) 233–254.

[41] G. Bakradze, L.P.H. Jeurgens, T. Acarturk, U. Starke, E.J. Mittemeijer, Atomic transport mechanisms in thin oxide films grown on zirconium by thermal oxidation, as-derived from O^{18}-tracer experiments, Acta Mater. 59 (2011) 7498–7507.

[42] G. Bakradze, L.P.H. Jeurgens, E.J. Mittemeijer, The different initial oxidation kinetics of Zr(0001) and Zr(10-10) surfaces, J. Appl. Phys. 110 (2011) 024904.

[43] Hauffe, High Temperature Oxidation of Metals, P. Kofstad John Wiley & Son, New York, 1966 340 S, Materials and Corrosion, 18 (1967) 956-957.

[44] E. Panda, L.P.H. Jeurgens, G. Richter, E.J. Mittemeijer, The amorphous to crystalline transition of ultrathin (Al,Mg)-oxide films grown by thermal oxidation of AlMg alloys: a high-resolution transmission electron microscopy investigation, J. Mater. Res. 25 (2010) 871–879.

[45] Y. Xu, X. Liu, L. Gu, J. Wang, P. Schützendübe, Y. Huang, Y. Liu, Z. Wang, Natural oxidation of amorphous Cu_xZr_{1-x} alloys, Appl. Surf. Sci. 457 (2018) 396–402.

[46] W. Kai, H.H. Hsieh, T.G. Nieh, Y. Kawamura, Oxidation behavior of a Zr-Cu-Al-Ni amorphous alloy in air at 300-425 °C, Intermetallics 10 (2002) 1265–1270.

[47] B. Wang, D.Y. Huang, N. Prud'homme, Z. Chen, F. Jomard, T. Zhang, V. Ji, Diffusion mechanism of Zr-based metallic glass during oxidation under dry air, Intermetallics 28 (2012) 102–107.

[48] F.J. Keneshea, D.L. Douglass, The diffusion of oxygen in Zirconia as a function of oxygen pressure, Oxid. Met. 3 (1971) 1–14.

[49] Y. Olshi, W.D. Klngery, Self-diffusion of oxygen in single crystal and polycrystalline aluminum oxide, J. Chem. Phys. 33 (1960) 480–486.

[50] G. Gutiérrez, B. Johansson, Molecular dynamics study of structural properties of amorphous Al_2O_3, Phys. Rev. B 65 (2002) 104202.

[51] X. Zhao, D. Ceresoli, D. Vanderbilt, Structural, electronic, and dielectric properties of amorphous ZrO_2 from ab initio molecular dynamics, Phys. Rev. B 71 (2005) 085107.

[52] B. Lee, B. Lee, A comparative study on hydrogen diffusion in amorphous and crystalline metals using a molecular dynamics simulation, Metall. Mater. Trans. A 45 (2014) 2906–2915.

[53] Z. Hu, Y. Xu, Y. Chen, P. Schützendübe, J. Wang, Y. Huang, Y. Liu, Z. Wang, Anomalous formation of micrometer-thick amorphous oxide surficial layers during high-temperature oxidation of $ZrAl_2$, J. Mater. Sci. Technol. 35 (2019) 1479–1484.